RESEARCH ARTICLE

NANO · MICRO small

www.small-journal.com

Dual-Encapsulated Highly Conductive and Liquid-Free Phase Change Composites Enabled by Polyurethane/Graphite Nanoplatelets Hybrid Networks for Efficient Energy Storage and Thermal Management

Minqiang Wu, Tingxian Li, Pengfei Wang, Si Wu, Ruzhu Wang, and Jie Lin*

Phase change materials (PCMs) are regarded as promising candidates for realizing zero-energy thermal management of electronic devices owing to their high thermal storage capacity and stable working temperature. However, PCM-based thermal management always suffers from the long-standing challenges of low thermal conductivity and liquid leakage of PCMs. Herein, a dual-encapsulation strategy to fabricate highly conductive and liquid-free phase change composites (PCCs) for thermal management by constructing a polyurethane/graphite nanoplatelets hybrid networks is reported. The PCM of polyethylene glycol (PEG) is first infiltrated into the cross-linked network of polyurethane (PU) to synthesize hybridized semi-interpenetrated composites (PEG@PU), and then incorporated with reticulated graphite nanoplatelets (RGNPs) via pressure-induced assembly to fabricate highly conductive PCCs (PEG@PU-RGNPs). The hybrid networks enable the PCCs to show excellent mechanical strength, liquid-free phase change, and stable thermal property. Notably, the dual-encapsulated PCCs exhibit high thermal and electrical conductivities up to 27.0 W m^{-1} K^{-1} and 51.0 S cm^{-1}, superior to the state-of-the-art PEG-based PCCs. Furthermore, the PCC-based energy device is demonstrated for efficient battery thermal management toward versatile demands of active preheating at a cold environment and passive cooling at a hot ambient. Overall, this work provides a promising route for fabricating highly conductive and liquid-free PCCs toward thermal management.

1. Introduction

Efficient energy storage and management attracts increasing concerns with the rapid industrial development, energy consumption, and growing population.[1] Thermal energy storage (TES) using phase-change materials (PCMs) has been developed as a promising technology to address the mismatch between thermal energy supply and demand.[2,3] Among various PCMs, organic polyethylene glycol (PEG) has drawn tremendous attention owing to its incomparable advantages, including high energy density, thermal and chemical stability, no toxicity, good biocompatibility, and low cost.[4,5] However, as the similar drawbacks of conventional solid-liquid PCMs, the leakage issues during the phase change process greatly restricts the wide application of PEG.[6] To solve this problem, one feasible solution is to modify PEG into polyurethane-based solid-solid PCMs using the chemical crosslinking method.[7,8] The PEG is chemically linked to the supporting material via different linkages such as urethane, ester, and ether modification.[9,10] In a typical cross-linked network of polyurethane (PU), PEG serves as a soft phase transition segment, and the hard segment of diisocyanates and chain extenders are responsible for avoiding the free flow of the soft segment during the phase change process. Despite the excellent shape-stabilized property and thermal stability of cross-linked solid-solid PCMs, the chemical or physical bunding of solid-solid PCM restricts the free movement of crystallizable soft parts, which results in the compromise of the TES capacity.[11,12]

Apart from the above-mentioned bottlenecks, the low thermal conductivity of pristine PCM is also a great concern for thermal charging/discharging. PEG-based PCMs typically have unsatisfied thermal conductivity ranging from 0.1 to 0.5 W m^{-1} K^{-1},[13] and thus hardly meet the high-power capacity demand.[14] To address this long-standing problem, intensive efforts have been dedicated by introducing high-conductivity fillers into the PCMs.[15] Among various high-conductivity fillers, carbon-based porous materials, such as graphite/graphene foam,[14,16] carbon

M. Wu, T. Li, P. Wang, S. Wu, R. Wang
Institute of Refrigeration and Cryogenics
School of Mechanical Engineering
Shanghai Jiao Tong University
Shanghai 200240, China
E-mail: Litx@sjtu.edu.cn

T. Li, R. Wang
Research Center of Solar Power and Refrigeration
Shanghai Jiao Tong University
Shanghai 200240, China

J. Lin
Department of Engineering Science
University of Oxford
Parks Road, Oxford OX1 3PJ, UK

The ORCID identification number(s) for the author(s) of this article can be found under https://doi.org/10.1002/smll.202105647.

DOI: 10.1002/smll.202105647

aerogel,[17] graphene aerogel,[18,19] carbon nanotube sponge[7,20,21] and expanded graphite (EG),[22,23] are frequently adopted to improve the thermal conductivity of PCMs by fabricating phase change composites (PCCs). Although the components of these porous fillers, such as graphene and carbon nanotube, exhibit ultrahigh intrinsic thermal conductivity (>1500 W m^{-1} K^{-1}[24]), only modest thermal conductivity enhancement of PCCs has been observed even at a high loading of additives due to the high thermal resistance between conductive fillers and adjacent PCMs.[14,25] Moreover, the unsatisfied thermal and mechanical stability of PCCs can also cause the degeneration of thermal conductivity during the phase transition process.[26] Additionally, the inherent shortcomings of conventional PCCs, such as high cost, low yield, and tedious preparation, hinder their extensive applications.[27] Hence, it is a great challenge to develop high-performance PCCs with high thermal conductivity, excellent thermal properties, and satisfying mechanical stability, for scalable thermal storage and management.

Herein, we report a dual-encapsulation strategy to fabricate highly conductive and liquid-free PEG-based PCCs. During the first encapsulation process, the PEG is infiltrated into the cross-linked network of PU to synthesize a highly hybridized semi-interpenetrated composite (PEG@PU). The 3D PU network endows the PEG to alleviate its leakage problem, and the inherent phase change property of PU also improves the thermal storage capacity of the PEG@PU composite. During the secondary encapsulation process, the PEG@PU composites are incorporated with reticulated graphite nanoplatelets (RGNPs) via facile pressure-induced assembly strategy to fabricate highly conductive PCCs (PEG@PU-RGNPs). The aligned layer-by-layer RGNPs network enables the PCCs to exhibit high thermal conductivity (27.0 W m^{-1} K^{-1}) and superior electrical conductivity (51.0 S cm^{-1}) at RGNPs loadings below 30 wt%. Furthermore, we demonstrate the PCC-based energy device for battery thermal management (BTM) toward the year-round versatile demands of passive cooling at high temperatures and active warm-up at low temperatures. The operating temperature of battery pack can be cooled below 55 °C even at a hot environment of 35 °C owing to the heat dissipation by the latent heat of the PCC during continuous high-rate charging/discharging cycles. On the other hand, the battery pack can be actively preheated by the electro-driven Joule heat of the PCC to maintain a moderate temperature range (35–40 °C) at a low ambient temperature of 0 °C, which increases the battery capacity by 13.5% compared with the bare battery pack. Therefore, our work provides a promising route to synthesize high-performance PCCs for various heat-related energy storage and thermal management for both heating and cooling demand.

2. Results and Discussion

2.1. Synthesis and Characterization of Dual-Encapsulated PCCs

Figure 1 shows the schematic illustration of the dual-encapsulation strategy for fabricating highly conductive and liquid-free PEG-based PCCs by constructing polyurethane/graphite nanoplatelets hybrid networks. One-step polymerization and in situ absorption methods are first adopted to synthesize highly hybridized semi-interpenetrated PEG@PU composite (a1 and a2 of Figure 1a). A certain amount of PEG and Hexamethylene Diisocyanate Biuret (HDIB) are respectively dissolved in *N*,*N*-dimethylformamide (DMF) under mechanical stirring at 60 °C to synthesize cross-linked PU network with nitrogen protection. When the solution became sticky, extra PEG solution is added quickly to be absorbed into the cross-linked PU network, and then the mixed solution is transferred to a vacuum oven at 60 °C for 24 h to obtain PEG@PU composite. The mass fraction of PEG in the PEG@PU composite is optimized as 70 wt% according to the liquid leakage proof testing (Figure S1, Supporting Information).

To enhance the thermal conductivity of PEG@PU composite, a facile pressure-induced assembly method is employed to fabricate highly conductive PEG@PU-RGNPs composites (Figure 1b). The PEG@PU composite is first freeze-pulverized into small particles with an average size of 20.2 μm (Figure S2, Supporting Information), and then these particles are mixed with EG matrix at a certain ratio. Subsequently, the mixtures are heated and stirred under 120 °C approximately 10 min to make the PEG@PU particles uniformly adhere to the surface of RGNPs inside porous EG (Figure S3, Supporting Information). The incompact composites of PEG@PU and RGNPs are then moved into a steel mold and compressed into a form-stable composite at 60 °C under the maximum compression pressure of 20 MPa. The mass fraction of RGNPs in PEG@PU-RGNPs composite is in a range of 5–30 wt% and the as-prepared composites are named as PCC-*x*, where *x* represents the mass fraction of RGNPs.

The microstructures of PEG@PU, EG, and PEG@PU-RGNPs are observed and compared. The PU has 3D network structure with numerous pores, which provides abundant space for the permeation of PEG, and the space of PU is occupied by the extra PEG for the PU@PEG composite (Figure S4, Supporting Information). The SEM image of PEG@PU exhibits a compact cross-section structure and irregular wrinkled strips caused by the crystallization of PEG segments (a2 of Figure 1a), demonstrating extra PEG is successfully infiltrated and occupies the void space of the 3D cross-linked PU network.[12,28] Figure 1c shows the thermally expanded worm-like EG is composed of numerous disordered RGNPs with van der Waals (vdW) interactions. The vdW interactions between adjacent RGNPs weaken the phonon scattering at the interface due to the adhesion energy, which contributes to reduce the interfacial thermal resistance and enhance the nanoscale thermal conduction.[23] After blending, the PEG@PU particles are readily adhered to EG and uniformly distributes on the surface of RGNPs (Figure 1d). The PEG@PU and EG composite is then compressed to prepare anisotropic PCCs at 60 °C. For the PEG@PU-RGNPs blocks, a compact layer-by-layer aligned RGNPs network is formed after compression (Figure 1e; Figure S5, Supporting Information), which contributes to the anisotropic thermal conductivity of the PCC block. In addition, the XPS spectrum reveals that the RGNPs are highly carbonized, and low oxygen content (1.07%) is observed after thermal expansion, which contributes to the conductivity enhancement of the PCC (Figure S6, Supporting Information).[29]

The FT-IR spectra of PEG, PEG@PU, EG, and PEG@PU-RGNPs are showed in Figure 1f. In the spectrum of PEG, the

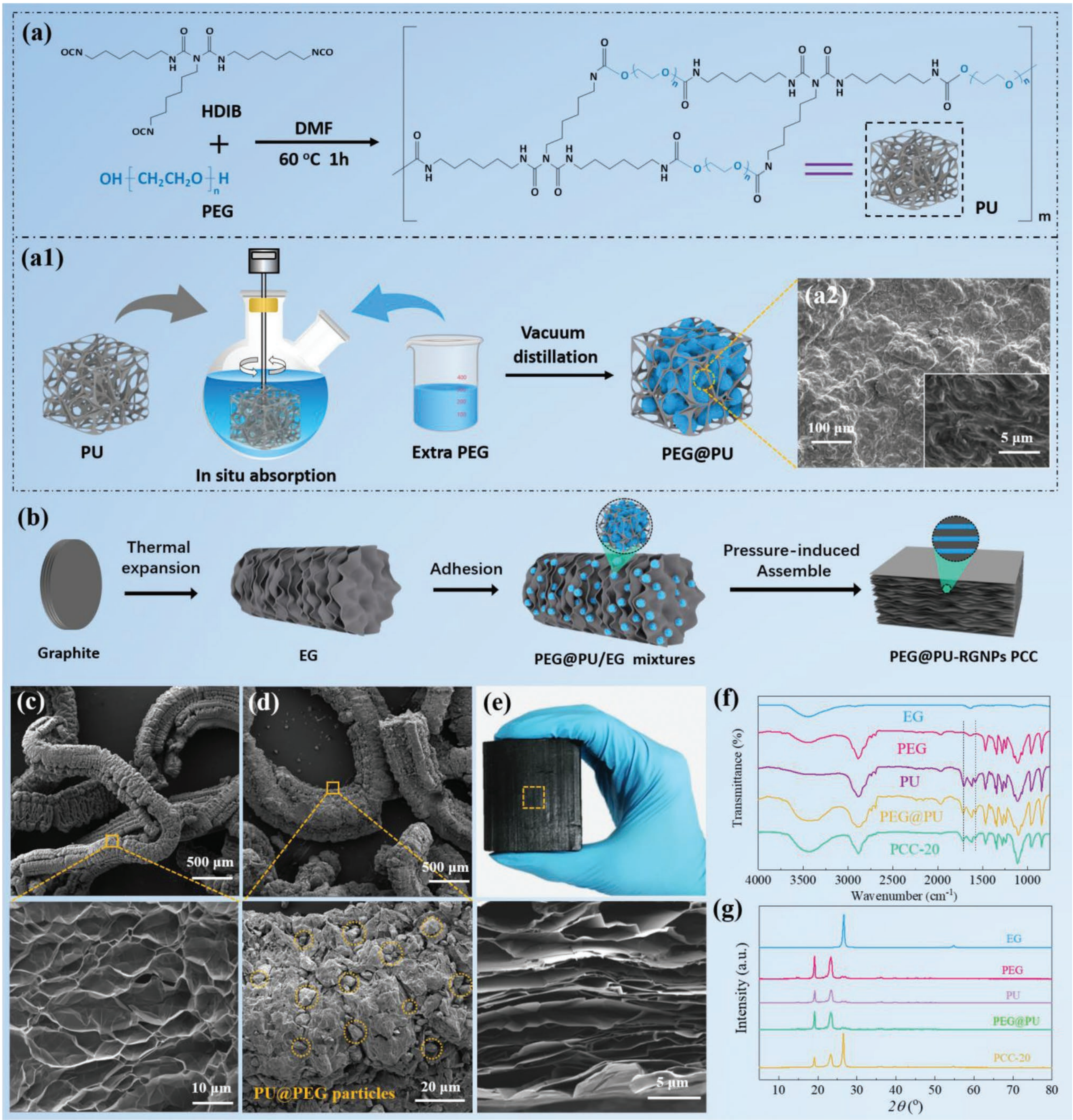

Figure 1. Dual-encapsulation processes for fabricating highly conductive and liquid-free PEG-based PCCs by constructing polyurethane/graphite nanoplatelets hybrid networks. a1–a3) The first encapsulation process for synthesizing highly hybridized semi-interpenetrated composites (PEG@PU) by infiltrating PEG into the cross-linked PU network. b) The secondary encapsulation process for preparing highly conductive PEG@PU-RGNPs PCCs by incorporating PEG@PU into RGNPs matrix via pressure-induced assembly and the enlarged image showing the microstructure of PEG@PU. c) SEM image of worm-like EG and its enlarged image showing the RGNP networks. d) SEM image of PEG@PU and EG mixtures and its enlarged image showing the PEG@PU particles adhered on the surface of RGNPs. e) Digital photograph of PEG-based PCC block (PEG@PU-RGNPs), and the enlarged cross-section image showing the layer-by-layer aligned RGNPs network after removing the PEG@PU from the PCC. f) Fourier-transform infrared spectroscopy (FT-IR) of EG, PEG, PEG@PU, and PEG@PU-RGNPs. g) X-ray diffraction (XRD) patterns of EG, PEG, PU, PEG@PU, and PEG@PU-RGNPs.

strong absorption peaks at 2878, 1468, 962, and 840 $\mathrm{cm^{-1}}$ are ascribed to C—H bonds, the peaks of —OH stretching vibration, and C—O—C symmetrical vibration appear at 3468 and 1106 $\mathrm{cm^{-1}}$, respectively. The characteristic absorption peaks of HDIB are observed at 3342, 2264, and 1678 $\mathrm{cm^{-1}}$, which are corresponding to the N—H, —NCO, and —NH—CO—NH— stretching vibration, respectively (Figure S7, Supporting Information). In the FT-IR spectrum of PEG@PU, after reaction, the peaks of —NCO and —NH—CO—NH— disappeared, while the emergence of new peaks at 1720 and 1533 cm^{-1} are attributed to the stretching vibration of —NHCOO— formed by the polymerization of HDIB and PEG.[30] In addition, the FT-IR spectrum of PEG@PU is similar to PU except for the stretching vibration of —OH at 3464 cm^{-1} of PEG, indicating the infiltration of PEG into the cross-linked PU network. Moreover, no new peaks are observed between spectra of EG, PEG@PU, and PEG@PU-RGNPs, suggesting that the dual-encapsulated PEG@PU-RGNPs is only a physical combination of PEG, PU, and RGNPs.

The crystalline phases of PEG, PU, EG, PEG@PU, and PEG@PU-RGNPs are analyzed by XRD as shown in Figure 1g. The sharp diffraction peaks of pristine PEG at 19.2° and 23.4° are ascribed to the lattice plane of (120) and $(1\bar{3}2)$, respectively. In the XRD curves of PU and PEG@PU, almost the same diffraction peaks at around 19.2° and 23.4° are observed as pristine PEG, which reveals that the crystallization property of the PEG in the cross-linked system does not change after polymerization with HDIB. The intensity of diffraction peaks proves that the crystalline regions of PEG in the PU have been decreased to some extent owing to the restriction caused by the crosslinking structure. However, the diffraction intensity of PEG@PU becomes stronger than that of PU, revealing that the crystallinity of PEG increases because of the additional PEG. Moreover, the XRD pattern of the PEG@PU-RGNPs is almost the sum of curves of EG and PEG@PU with a reduction in the intensity for all three peaks, representing the physical combination of the RGNPs and the PEG@PU. Notably, these results are further validated by the following DSC experiment.

2.2. Thermal Performance and Stability of PCCs

Figure 2 shows the thermal performance and stability of PEG@PU-RGNPs PCCs. The phase change enthalpies and temperatures of PEG@PU-RGNPs are characterized by differential scanning calorimetry (DSC). After reacting with HDIB, PU shows an inherent phase change enthalpy (ΔH_m) of 120.6 J g^{-1} and decreased melting temperature (T_m) of 43.4 °C, resulting from chemical restriction and physical entanglements (Table S1, Supporting Information).[30] The ΔH_m and T_m of PEG@PU composites become high with increasing extra PEG loading (Figure S8, Supporting Information), and the PEG@PU with 70 wt% PEG loading possesses a ΔH_m of 163.5 J g^{-1} and T_m of 46.5 °C, which is superior to the previously reported PEG-based PCMs with T_m ranges of 35–65 °C (Table S2, Supporting Information). Figure 2a presents the DSC results of PCCs and the corresponding data is also summarized in Table S3, Supporting Information. After the inclusion of PEG@PU within RGNPs, no significant changes of T_m and freezing temperature (T_c) are observed, demonstrating that the effective physical combination of RGNPs has no significant effect on the melting and crystallization of PEG@PU.[7] However, the phase change enthalpies of PCCs are suppressed as the increase of RGNPs content since RGNPs have no effective phase change behavior at the temperature around 50 °C.

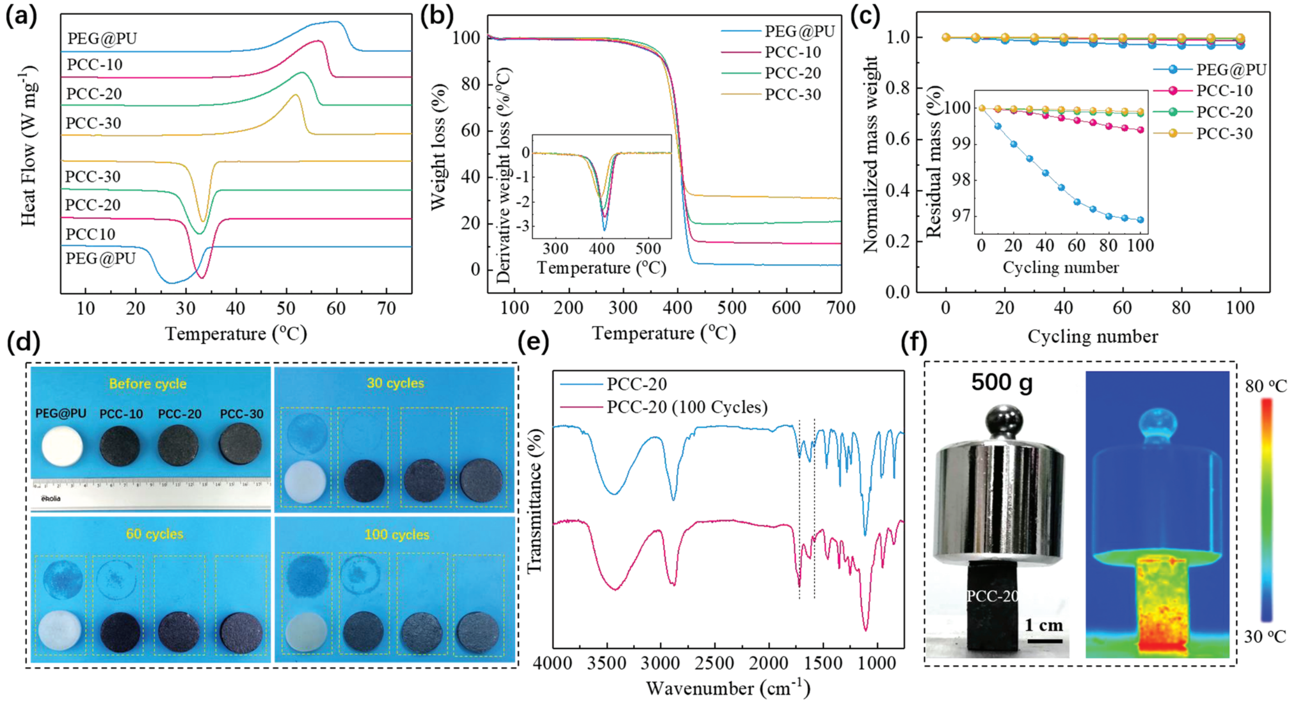

Figure 2. Thermal performance and stability of PEG@PU-RGNPs PCCs. a) The DSC curves of PEG@PU and PEG@PU-RGNPs composites. b) TGA and corresponding DTG curves of PEG@PU and PEG@PU-RGNPs composites. c) The weight loss of PEG@PU and PEG@PU-RGNPs PCCs at different cycling times. d) Digital images of PEG@PU, PCC-10, PCC-20, and PCC-30 during 100 times thermal cycling test. e) FT-IR spectra of PCC-20 before and after 100 thermal cycles. f) Mechanical strength test of PCCs at a temperature higher than the phase-change temperature of PEG. The PCC sample was heated on a heating panel with constant temperature of 80 °C.

Thermal degradation of PEG@PU and PCCs are measured by TGA as shown in Figure 2b. The detailed data are summarized in Table S4, Supporting Information. The thermal degradation of the PEG@PU, PCC-10, PCC-20, and PCC-30 samples all involve two steps. In the first step, about 5% weight loss occurred at the temperature range of 280–360 °C due to the degradation of the urethane segment in the PU molecular chains. The second degradation stage appears in a range from 365 to 430 °C due to the decomposition of PEG.[31] A slight decrease in degradation temperature of maximum weight loss rate is observed as the RGNPs loading increases. This phenomenon occurs mainly because the thermal conductivity of the PCC is improved as the improvement of RGNPs loading, which promotes the internal heating rate of the PCC. In addition, the amount of char yielding at the maximum temperature for PEG@PU and PCCs are 2.1%, 11.4%, 21.5%, and 31.0%, respectively, which is consistent with the mass fraction of RGNPs in the composites. Notably, no significant degradation occurs below the melting temperature of the PCCs.

The thermal stability of the PCC during long-term operation in a harsh working environment is also examined. Figure 2c shows the comparison of the weight losses of PEG@PU, PCC-10, PCC-20, and PCC-30 samples during the 100 times endothermic and exothermic cycles under the temperature range of 25–100 °C. The PEG@PU shows a significant weight loss in the first 60 cycles, while the trend is eased after 80 cycles. The final weight loss of PEG@PU is around 3.1%, indicating the leakage phenomenon of PEG is greatly alleviated after the first encapsulation of PU. Notably, the final weight losses of PCC-10, PCC-20, and PCC-30 are reduced to 0.6%, 0.15%, and 0.09%, respectively, demonstrating the successful encapsulation of PEG@PU within RGNPs networks further alleviates the leakage problem of PEG. On the other hand, there is no significant evolution of the phase change enthalpy of PCC-20 during the melting and freezing process (Figures S9 and S10, Supporting Information). The FT-IR spectra of PCC-20 after 100 thermal cycles is highly consistent with the original PCC (Figure 2e), indicating a stable chemical structure of the PCC-20. Moreover, our PCC blocks also exhibit low thermal expansion (<0.5%), enhanced mechanical property and excellent mechanical stability during the phase transition process (Figure 2f; Figure S11, Supporting Information). These results show no significant thermal or chemical degradation occurs during the long-term thermal cycling process, which indicates the excellent thermal stability of PCCs.

2.3. Thermal and Electrical Conductivities and Energy Conversion Performance

Figure 3 shows the thermal and electrical conductivities of PEG@PU-RGNPs PCCs. Thermal conductivity (K) of PCCs is an important parameter, which determines the thermal power during the charging/discharging process. PEG and PEG@PU have a low thermal conductivity of 0.26–0.35 W m^{-1} K^{-1}, while the PCCs exhibit the anisotropic and highly enhanced thermal conductivities due to the introduction of highly conductive layered RGNPs network as observed by SEM (Figure 3a). Both axial and radial thermal conductivities of PCCs increase with increasing RGNPs loading. Specifically, the PCC-30 shows radial thermal conductivity as high as 27.0 W m^{-1} K^{-1}, which is about 102 times higher than the pristine PEG. The high thermal conductivity enhancement of the resultant PEG@PU-RGNPs composites can be explained by two mechanisms. First, different from conventional preparation methods,[32–35] the inherent large-size RGNPs structure of the EG matrix has maintained to construct large-scale heat transfer pathways.[36] On the other hand, the interfacial thermal resistance between adjacent RGNPs and PCM in the compact PCCs can be greatly reduced by employing pressure-induced directional compression assemble strategy, which thus boost the transmission of phonons and reduce the overall thermal resistance.[5,23,37] Although many previous results demonstrated that carbon-based additives can enhance the thermal conductivities of PCMs, the thermal conductivity enhancement shows a huge difference even using the same additive and loading content.[7,19,28,38–41] Besides, the fabrication of PCCs with high additive content is still challenging by using conventional methods.[42]

To further reveal the effect of different thermal conductivities on the heat transfer performance of PCCs, transient temperature responses of the PEG@PU and PEG@PU-RGNPs composites are recorded. As shown in Figure 3b, the temperature evolution curves of PEG@PU and PCCs show that the thermal response becomes more sensitive and the incremental rate of temperature becomes faster with increasing RGNPs loading, indicating the combination of RGNPs significantly enhances the heat transfer performance of PCCs. The infrared images further demonstrate the enhanced heat diffusion capability of the PCCs (Figure S12, Supporting Information). In addition to the thermal conductivity, thermal effusivity is another important parameter, which represents the overall thermal energy exchange capacity of the PCCs.[43]

$$e = \sqrt{K\rho\Delta H} \tag{1}$$

where ρ and ΔH are the bulk density and phase change enthalpy of PCC.

Figure 3c and Table S5, Supporting Information, shows the comparison of the thermal effusivities between the as-synthesized PEG@PU-RGNPs and the reported PEG-based PCCs from the different literatures.[7,31,41,44–53] Our PCCs not only exhibit superior thermal conductivities, but also display higher thermal effusivities, which ensures the high-efficient heat exchange capability. In addition to the PEG-based PCCs, our PEG@PU-RGNPs PCCs also exhibit higher thermal conductivity enhancement compared with reported non-PEG-based PCCs (Figure S13 and Table S6, Supporting Information).

Recently, electro-thermal conversion and storage based on functional PCCs has shown great potential in the thermal energy management of electronic devices, power vehicles, and off-peak electricity storage systems.[15,54–56] The thermal conductivity and electrical conductivity of PCC are two main factors affecting their electro-thermal conversion performance. Figure 3d shows the layered RGNPs not only serve as a highly conductive matrix but also provide a conductive percolation network to enhance the electrical conductivity of PCCs. Similar to the thermal conductivity, an anisotropic electrical conductivity

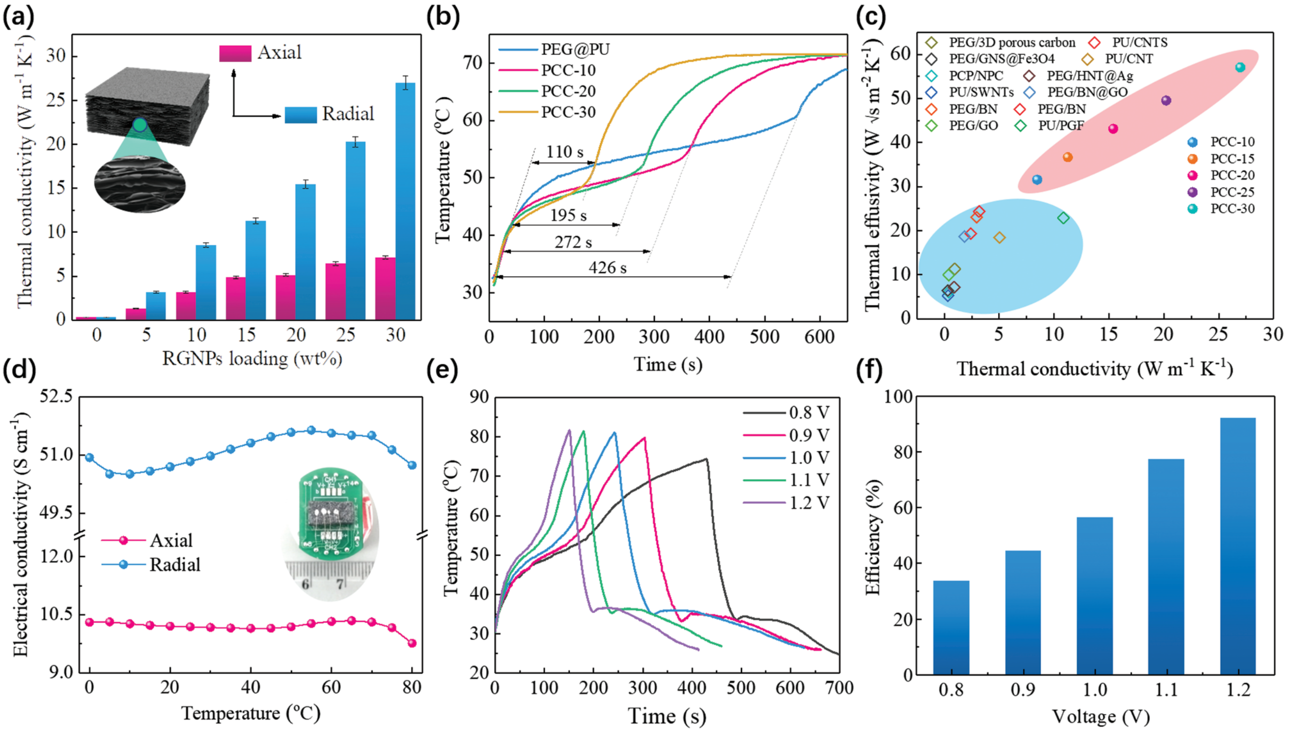

Figure 3. Thermal and electrical conductivities of PEG@PU-RGNPs PCCs. a) The anisotropic thermal conductivities of PCCs at different RGNPs contents. b) Time-temperature curves of PEG@PU, PCC-10, PCC-20, and PCC-30 samples under a constant heating temperature of 80 °C. c) A comparison of the thermal effusivity and thermal conductivity of PCCs from the latest reported PEG/PU-based PCCS.[7,31,41,44–53] Note: some reports did not mention the density of the PCC, thus we calculate the probably maximum thermal effusivity of the PCCs by using the maximum density of the composite block, assuming the PCM and carbon matrix are perfectly mixed and there are no pores existing inside the composite blocks. d) Anisotropic effective electrical conductivity of the PCC-20 at different working temperatures, the inset showing the digital photo of PCC-20 sample for electric conductivity test. e) Time-temperature evolution curves of the PCC-based electro-thermal conversion and storage device during the charging and discharging processes. f) Electro-thermal conversion efficiencies of the PCC-based electro-thermal conversion and storage device at different voltages.

of PCC-20 is observed, where the radial electrical conductivity (51 S cm^{-1}) is about 4 times higher than the axial one (10 S cm^{-1}) at the temperature range of 0–80 °C. Subsequently, the PCC-20 samples are subjected to a constant voltage (0.8–1.2 V) along the radial direction to perform electro-thermal conversion and storage. As shown in Figure 3e, the temperatures of PCCs increase rapidly at the initial stage until to a plateau with small slope at T_m of 44 °C, indicating the generated Joule heat is stored by the latent heat of PCC.[7] After the energy storage is completed, another rapid temperature rise appears and drops sharply when the power supply is cut off. During the natural cooling process, the second temperature plateau at T_c of 35 °C is associated with the crystallization of PCCs. These values of the phase-change plateau during the electro-driven heating and cooling processes are constant with the DSC results discussed above (Figure 2a; Table S3, Supporting Information). Besides, the phase-change duration of the heating plateau is greatly shortened with increasing driving voltage. The electro-thermal conversion efficiency of PCC-20 increases from initially 33.6% to the maximum value of 92.1% as the driving voltage rising to 1.2 V (Figure 3f). The elevation of energy conversion efficiency at higher voltage is mainly attributed to the fact that higher voltage shortens the phase-change duration and thus ultimately suppresses convective and radiative heat losses to the environment.

2.4. PCC-based Battery Thermal Management

We further demonstrate the PCC-based energy device for the year-round BTM using commercial 18650 lithium-ion batteries (LiBs) by utilizing the superior thermal properties and electro-thermal conversion and storage of PEG@PU-RGNPs composites (**Figure 4**; Figure S14, Supporting Information). Figure 4a shows the concept design of PCC-based BTM for both preheating and cooling demands of LiBs. When the battery is exposed to low-temperature environment, the LiB is preheated at the start-up stage by the Joule heat generated from the electro-thermal conversion of the PCC, and the latent heat of PCC during the crystallization process provides a long-time warm-up of the LiBs. By contrast, in a high-temperature environment, the heat released by LiB is absorbed by the PCC in the form of latent heat through its phase transition to maintain an optimum operating temperature, and thus preventing the risks of capacity loss, lifespan shortening, and even thermal runaway of the LiBs.

Two LiB packs with and without PCC-20 block wrap are tested to verify the feasibility of the PCC-based BTM under a low-temperature environment. A low voltage is applied to the PCC to perform electro-thermal-driven preheating of the wrapped LiB pack via the electro-thermal conversion of PCC blocks before initiating the LiB charge/discharge. Figure 4b

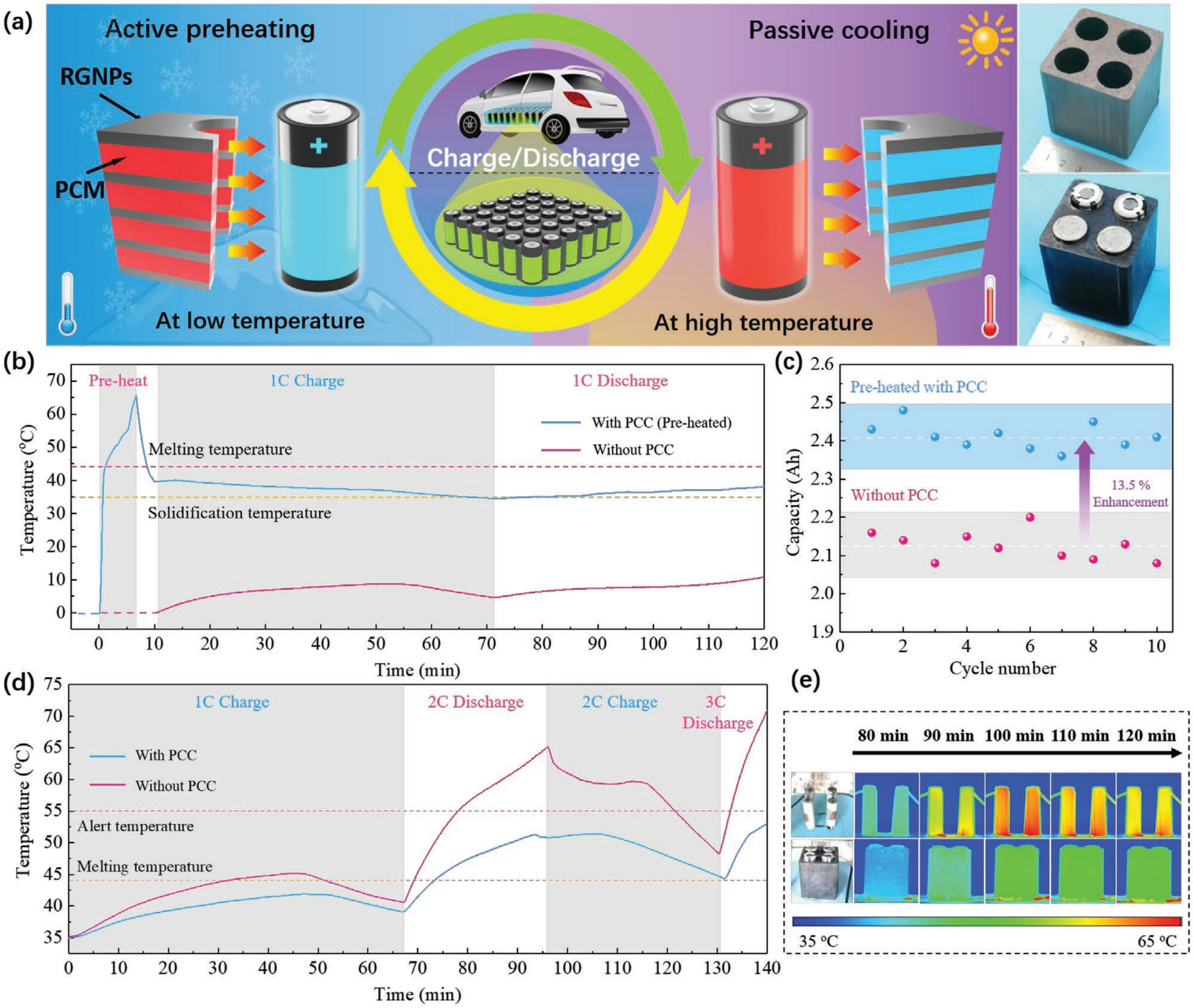

Figure 4. Demonstration of the PCC-based BTM for both preheating and cooling demands. a) Schematic of PCC-based BTM for electro-thermal-driven active preheating at low temperature and phase-change-driven passive cooling at high temperature. The digital images at the right side are the LiB pack wrapped with the PCC block. b) Comparison of temperature evolution curves of the LiB packs with and without PCC warm-up at a cold environment (0 °C). c) Comparison of the effective energy capacities of the LiB packs with and without PCC-based active warm-up. d) Comparison of temperature evolution curves of the LiB packs with and without PCC cooling at a hot environment (35 °C). e) Digital photos of LiB packs with and without PCC wrap and the corresponding infrared images during charge/discharge process.

displays the temperature evolution curves of LiB packs with and without the PCC-based BTM at low ambient temperature (0 °C). For the PCC-wrapped LiB pack, a sharp temperature rise is observed at the initial period during electrical-driven preheating process. As the applying voltage continues, the temperature rise slows down at 45 °C until another sharp temperature slope appears starting from 55 °C, indicating the completion of the phase-change process of the PCC. After the termination of electrical preheating process, the temperature of the LiB pack decreases until reaches a second plateau with a minimum slope at around 39 °C. The temperature evolution trend of LiB pack is consistent with the DSC and electro-thermal conversion results of PCCs, demonstrating the LiB pack can be effectively preheated by the PCC through the electro-thermal conversion. During the successive 1C charge/discharge process, a relatively mild temperature curve is observed in the range of 34–40 °C. In contrast, the bare LiB pack without warm-up always suffers from the low operating temperature (0–11 °C) during the continuous charge/discharge process. These results indicate that a stable and optimum working temperature of the LiB pack can be provided by releasing the latent heat of the PCC in a low-temperature environment.

Furthermore, it was commonly accepted that operating LiBs at high temperatures should be avoided due to the concerns of accelerated degradation and possible thermal runaway. However, recent studies revealed that preheating LiBs at the charging stage via finite exposure to an elevated temperature can remarkably improve the rate capability and cycle life, especially from a cold start.[57–59] As a result, the effective charge capacity of the LiB pack with active preheating of the PCC wrap is improved by 13.5% compared with the bare LiB pack after 10 cycles at 0 °C (Figure 4c).

In addition to the electro-thermal-driven active preheating of the LiB pack in a cold environment, the phase-change-driven passive cooling performance of PCC is also examined. During the passive cooling test, two LiB packs with and without PCC wrap are adopted to perform consecutive charge/discharge at a hot temperature of 35 °C. As illustrated in Figure 4d, two LiB packs show similar temperature evolution trends. However, the temperature of PCC-wrapped LiB is far lower than that of non-wrapped one, especially during the high charging/discharging rate. For example, the maximum temperatures of bare LiB reach 65 °C and even 70 °C under 2C and 3C discharging processes, while that of wrapped LiB pack remains a moderate temperature range even at high charging/discharging process, much lower than the alarming temperature (55 °C). This is mainly contributed to the high thermal conductivity and TES capacity of the PCC wrap, where the heat generated from LiB rapidly transfers to the PCC through the internal high-conductive RGNPs networks and then stores in the form of latent heat of PEG. Moreover, compared with the bare LiB pack, the infrared image shows that the battery pack with PCC wrap has a uniform temperature distribution (Figure 4e), which further demonstrates the superior cooling performance of the PCC.

3. Conclusion

In summary, we report a dual-encapsulation strategy to fabricate highly conductive and liquid-free PEG-based PCCs for thermal management by constructing PU and RGNPs hybrid networks inside PCCs. The cross-linked 3D PU network alleviates the liquid leakage of PEG and the resultant highly hybridized PEG@PU exhibits an enlarged latent heat of 163.5 J g^{-1}. The aligned layer-by-layer RGNPs network not only further improves the thermal stability of PCCs, but also enables the PCCs to have tailored thermal conductivities of 3.1–27.0 W m^{-1} K^{-1} at RGNPs loadings of 5–30 wt%, superior to the state-of-the-art PEG-based PCCs. Meanwhile, the resultant PCC also exhibits superior electrical conductivity (51.0 S cm^{-1}) and efficient electro-thermal conversion and storage (≈92.1%) under a low applying voltage of 1.2 V. We further demonstrate a PCC-based BTM toward the year-round versatile demands of cooling at high temperatures and preheating at low temperatures. The PCC-based BTM shows that a moderate working temperature range can be provided through electro-thermal-driven active preheating under cold environment or phase-change-driven passive cooling under hot environment during high-rate charge/discharge cycles. Overall, our works provide a promising scalable method for synthesizing high-performance PCCs and pave a way for the versatile thermal management of electronics toward both warm-up and cooling demands.

4. Experimental Section

Materials: Polyethylene glycol (PEG, AR, $M_n = 4000$ g mol^{-1}) purchased from Sinopharm Chemical Reagent Co., Ltd. was first dried under vacuum at 80 °C for 24 h. *N*,*N*-Dimethylformamide (DMF, AR) obtained from Beijing Chemical Works, China, was distilled under vacuum after refluxed and stirred overnight. Hexamethylene Diisocyanate Biuret (HDIB, N75, with NCO% = 15.6%) purchased from Bayer, Germany, was used as received. Graphite flakes intercalation compounds (mesh 50) were purchased from Shanghai Yi Fan Graphite Co. Ltd. They were washed with absolute ethanol several times and dried under vacuum at 60 °C for 3 h. Graphite flakes were heated to 750 °C for about 15 min to prepare long and loose worm-like EG with orderly hierarchical structures.

Preparation of PEG@PU Composites: The PEG@PU composites were synthesized in flame-dried flask through a one-step polymerization and an in situ doping method, respectively. Typically, a certain amount of PEG and HDIB (3:2 molar ration of PEG/HDIB) were respectively dissolved in DMF under mechanical stirring at 60 °C and protected with nitrogen. When the solution became sticky, a certain amount of extra PEG was added quickly. The cross-linking PU network absorbed the PEG and solvent rapidly. After completion, the composite solution was transferred to a vacuum oven at 60 °C for 24 h to get the PEG@PU. The mass fraction of PEG in PEG@PU composites was optimized as 70 wt% according to the leakage proof testing.

Preparation of PEG@PU-RGNPs Composites: A facile pressure-induced assemble method was employed to fabricate highly conductive phase change composites (PCCs) of PEG@PU-RGNPs. Typically, the pulverized PEG@PU microparticles were mixed with EG at a certain ratio and vigorously stirred and then heated to 120 °C for approximately 10 min to make the PEG@PU microparticles uniformly adhere to the surface of RGNPs of EG. The incompact PEG@PU-RGNPs composites were then moved into a home-made steel mold and compressed into shaped composite at 60 °C under the maximum compression pressure of 20 MPa. The mass fraction of RGNPs in PEG@PU-RGNPs composites were in a range of 5–30 wt% and the as prepared composites were named as PCC-*x*, where *x* represents the mass fraction of RGNPs.

Characterization: The sample morphology and structure were characterized using SEM (Sirion 200, USA) equipped with energy disperse spectroscopy (EDS, INCA X-Act). The element composition of EG was measured by X-ray photoelectron spectroscopy (XPS) on a Model K-Alpha instrument (ThermoFisher Scientific Company, USA) using a monochromated Al Kα source and a pass energy of 50 eV at a base pressure of 1×10^{-8} mbar. XRD patterns were measured with a Poly-functional X-ray diffractometer (3 kW/*D8 ADVANCE DAVINCI, Germany) to determine the crystalloid phase of the composites. FT-IR absorption spectroscopy was obtained via (Nicolet 6700, USA) to analyze the chemical structure of composites. Phase-transition temperature, latent heat, specific heat capacity, and cycling enthalpy were tested by differential scanning calorimeter (DSC, Perkin-Elmer, USA) at a scanning rate of 5 °C min^{-1} under flowing nitrogen (flow rate: 100 mL min^{-1}). Samples were accurately weighted (ranging from 5 to 10 mg) and then sealed in aluminum pans. Hot Disk thermal constants analyzer (TPS3500, Hot Disk AB Company, Sweden) was adopted to calculate the thermal conductivity of PCCs in axial and radial directions. Thermal decomposition curves (TGA) were carried out with a thermogravimetric analyzer (Pyris 1, USA) at a heating rate of 10 °C min^{-1} under N_2 atmosphere. The resistivity measurement of PCC was carried out by a physical property measurement system (PPMS-9T(EC-II), Quantum Design, USA). The operating temperature range was 0–80 °C with a heating rate of 5 °C min^{-1}.

Thermal Conductivity Measurement: The axial and radial thermal conductivities of PCC blocks (K_a and K_r) were measured by using Hot Disk thermal constant analyzer (TPS 3500, Hot Disk AB Company, Sweden). The accuracy of the thermal conductivity is within ±3%. The thermal conductivity was calculated with the equation $K = a \times C_p \times \rho$, where a is the thermal diffusivity, C_p the specific heat capacity, and ρ the density of samples. All samples were fabricated with diameter of 30 mm and thickness of 15 mm, the thermal conductivity of each sample was derived from the average value of three measurements.

Thermal Cycling Tests: Thermal cycling testing of as prepared PEG@PU and PEG@PU/RGNPs was performed in a furnace with forced air cooling. The thermal cycling consists of heating the samples to 100 °C for 10 min, and then cooling to room temperature (25 °C) by forced natural convection. The mass weights of samples were recorded before and after thermal cycling, and the cycling tests were undertaken for up to 100 cycles.

Electro-Thermal Energy Conversion and Storage: The electro-thermal energy conversion and storage testing was implemented with DC power. A rectangular shape PCC sample was connected to the DC power with copper clip, and the conductive silver-glue paste was used to ensure the good electronic conduction. A certain voltage (0.8–1.2 V) was applied to the PCC samples by the DC power. RTD temperature sensor (Pt100) was attached to the PCC samples to measure the temperature evolution in situ during the electro-heating and natural cooling processes. The electro-thermal conversion efficiency was calculated by using Equation (2).

$$\eta = \frac{m\Delta H}{UIt} \tag{2}$$

where m is the weight of the PCC sample, ΔH is the phase change enthalpy of PCC sample, and the U, I, and t are the voltage, current and time duration of phase transition, respectively. The phase change duration was calculated by drawing the tangent of time-temperature evaluation curve after phase transition.

Battery Thermal Management Experiments: The commercial 18650 lithium-ion battery (LiB) monomers were adopted to examine the feasibility of thermal management by used the PCC-based energy device. The main working parameters of the LiB included the rated capacity of 2600 mAh, nominal voltage of 3.7 V, voltage upper limit of 4.2 V and voltage lower limit of 2.5 V. Two LiB packs (LiB cells × 4) were comparatively tested with a battery charging/discharging test system under the same ambient temperatures (T_a). One LiB pack was wrapped with rectangle PEG@PU-RGNPs block, and the other was exposed to the ambient. During the LiB preheating (T_a = 0 °C) tests, a certain voltage was applied to the PEG@PU-RGNPs block through square copper electrode that tightly attached to both sides of the block to perform the electro-driven preheating of LiB pack. Once the electro-driven phase transition of PEG@PU-RGNPs block completed, the electric heating was stopped and the block was naturally cooled to a steady temperature around 40 °C before starting the cyclic charge/discharge of LiB pack. During LiB cooling (T_a = 35 °C) tests, a continuous charge/discharge process was performed for both two LiB packs. The average temperature evolution of LiB packs was monitored with RTD temperature sensors (PT100 × 4) attached to the surface of 4 cells during preheating and cooling tests.

Supporting Information

Supporting Information is available from the Wiley Online Library or from the author.

Acknowledgements

This work was supported by the National Natural Science Foundation of China under the contract no. 51876117 and the National Key R&D Program of China under the contract no. 2018YFE0100300.

Conflict of Interest

The authors declare no conflict of interest.

Data Availability Statement

The data that support the findings of this study are available from the corresponding author upon reasonable request.

Keywords

battery thermal management, phase change composites, reticulated graphite nanoplatelets, thermal conductivity, thermal storage

Received: September 17, 2021
Revised: November 4, 2021

---

[1] D. Tilman, R. Socolow, J. A. Foley, J. Hill, E. Larson, L. Lynd, S. Pacala, J. Reilly, T. Searchinger, C. Somerville, *Science* **2009**, *325*, 270.
[2] C. Liu, F. Li, L. P. Ma, H. M. Cheng, *Adv. Mater.* **2010**, *22*, E28.
[3] C. Liu, Z. Rao, J. Zhao, Y. Huo, Y. Li, *Nano Energy* **2015**, *13*, 814.
[4] M. K. Rathod, J. Banerjee, *Renewable Sustainable Energy Rev.* **2013**, *18*, 246.
[5] M. Wu, S. Wu, Y. Cai, R. Wang, T. Li, *Energy Storage Mater.* **2021**, *42*, 380.
[6] Y. Ahmadi, K. Kim, S. Kim, M. Tabatabaei, *Energy Storage Mater.* **2020**, *30*, 74.
[7] W. Aftab, A. Mahmood, W. Guo, M. Yousaf, H. Tabassum, X. Huang, Z. Liang, A. Cao, R. Zou, *Energy Storage Mater.* **2019**, *20*, 401.
[8] T. Qian, J. Li, X. Min, W. Guan, Y. Deng, L. Ning, *J. Mater. Chem. A* **2015**, *3*, 8526.
[9] S. Sundararajan, A. B. Samui, P. S. Kulkarni, *J. Mater. Chem. A* **2017**, *5*, 18379.
[10] Y. Kou, K. Sun, J. Luo, F. Zhou, H. Huang, Z.-S. Wu, Q. Shi, *Energy Storage Mater.* **2021**, *34*, 508.
[11] Y. Zhou, X. Wang, X. Liu, D. Sheng, F. Ji, L. Dong, S. Xu, H. Wu, Y. Yang, *Carbon* **2019**, *142*, 558.
[12] Y. Zhang, L. Wang, B. Tang, R. Lu, S. Zhang, *Appl. Energy* **2016**, *184*, 241.
[13] Y. Wei, J. Li, F. Sun, J. Wu, L. Zhao, *Green Chem.* **2018**, *20*, 1858.
[14] H. Ji, D. P. Sellan, M. T. Pettes, X. Kong, J. Ji, L. Shi, R. S. Ruoff, *Energy Environ. Sci.* **2014**, *7*, 1185.
[15] K. Yuan, J. Shi, W. Aftab, M. Qin, A. Usman, F. Zhou, Y. Lv, S. Gao, R. Zou, *Adv. Funct. Mater.* **2020**, *30*, 1904228.
[16] J. Yang, G. Qi, R.-Y. Bao, K. Yi, M. Li, L. Peng, Z. Cai, M.-B. Yang, D. Wei, W. Yang, *Energy Storage Mater.* **2018**, *13*, 88.
[17] X. Huang, W. Xia, R. Zou, *J. Mater. Chem. A* **2014**, *2*, 19963.
[18] B. Mu, M. Li, *Sci. Rep.* **2018**, *8*, 1.
[19] P. Min, J. Liu, X. Li, F. An, P. Liu, Y. Shen, N. Koratkar, Z. Z. Yu, *Adv. Funct. Mater.* **2018**, *28*, 1805365.
[20] L. Chen, R. Zou, W. Xia, Z. Liu, Y. Shang, J. Zhu, Y. Wang, J. Lin, D. Xia, A. Cao, *ACS Nano* **2012**, *6*, 10884.
[21] Z. Zheng, J. Jin, G.-K. Xu, J. Zou, U. Wais, A. Beckett, T. Heil, S. Higgins, L. Guan, Y. Wang, *ACS Nano* **2016**, *10*, 4695.
[22] L. Xia, P. Zhang, R. Wang, *Carbon* **2010**, *48*, 2538.
[23] S. Wu, T. Li, Z. Tong, J. Chao, T. Zhai, J. Xu, T. Yan, M. Wu, Z. Xu, H. Bao, *Adv. Mater.* **2019**, *31*, 1905099.
[24] A. A. Balandin, *Nat. Mater.* **2011**, *10*, 569.
[25] M. Shtein, R. Nadiv, M. Buzaglo, K. Kahil, O. Regev, *Chem. Mater.* **2015**, *27*, 2100.
[26] R. Zheng, J. Gao, J. Wang, G. Chen, *Nat. Commun.* **2011**, *2*, 1.
[27] W. Aftab, X. Huang, W. Wu, Z. Liang, A. Mahmood, R. Zou, *Energy Environ. Sci.* **2018**, *11*, 1392.
[28] Y. Zhou, X. Liu, D. Sheng, C. Lin, F. Ji, L. Dong, S. Xu, H. Wu, Y. Yang, *Thermochim. Acta* **2017**, *658*, 38.
[29] W. Dai, T. Ma, Q. Yan, J. Gao, X. Tan, L. Lv, H. Hou, Q. Wei, J. Yu, J. Wu, *ACS Nano* **2019**, *13*, 11561.
[30] Y. Zhou, X. Liu, D. Sheng, C. Lin, F. Ji, L. Dong, S. Xu, H. Wu, Y. Yang, *Chem. Eng. J.* **2018**, *338*, 117.

[31] Y. Wang, B. Tang, S. Zhang, *Adv. Funct. Mater.* **2013**, *23*, 4354.
[32] M. Buzaglo, I. P. Bar, M. Varenik, L. Shunak, S. Pevzner, O. Regev, *Adv. Mater.* **2017**, *29*, 1603528.
[33] F. Wang, J. Yi, Y. Wang, C. Wang, J. Wang, Y. Xia, *Adv. Energy Mater.* **2014**, *4*, 1300600.
[34] Z. Zhang, G. Alva, M. Gu, G. Fang, *Energy* **2018**, *157*, 625.
[35] W. Li, W. Cheng, B. Xie, N. Liu, L. Zhang, *Energy Convers. Manage.* **2017**, *149*, 1.
[36] J. Yang, Y. Yang, S. W. Waltermire, X. Wu, H. Zhang, T. Gutu, Y. Jiang, Y. Chen, A. A. Zinn, R. Prasher, *Nat. Nanotechnol.* **2012**, *7*, 91.
[37] T. Li, M. Wu, S. Wu, S. Xiang, J. Xu, J. Chao, T. Yan, T. Deng, R. Wang, *Nano Energy* **2021**, *89*, 106338.
[38] M. Mehrali, S. T. Latibari, M. Mehrali, T. M. I. Mahlia, H. S. C. Metselaar, M. S. Naghavi, E. Sadeghinezhad, A. R. Akhiani, *Appl. Therm. Eng.* **2013**, *61*, 633.
[39] I. Kholmanov, J. Kim, E. Ou, R. S. Ruoff, L. Shi, *ACS Nano* **2015**, *9*, 11699.
[40] S. Wang, P. Qin, X. Fang, Z. Zhang, S. Wang, X. Liu, *Sol. Energy* **2014**, *99*, 283.
[41] Y. Lv, W. Zhou, W. Jin, *Energy Build.* **2016**, *111*, 242.
[42] S. Wu, T. Li, M. Wu, J. Xu, Y. Hu, J. Chao, T. Yan, R. Wang, *J. Mater. Chem. A* **2020**, *8*, 20011.
[43] H. Lei, C. Fu, Y. Zou, S. Guo, J. Huo, *J. Mater. Chem. A* **2019**, *7*, 6720.
[44] W. Wu, X. Huang, K. Li, R. Yao, R. Chen, R. Zou, *Appl. Energy* **2017**, *190*, 474.
[45] J. Shi, W. Aftab, Z. Liang, K. Yuan, M. Maqbool, H. Jiang, F. Xiong, M. Qin, S. Gao, R. Zou, *J. Mater. Chem. A* **2020**, *8*, 20133.
[46] D. G. Atinafu, W. Dong, X. Huang, H. Gao, J. Wang, M. Yang, G. Wang, *Sol. Energy Mater. Sol. Cells* **2018**, *179*, 392.
[47] S. Song, F. Qiu, W. Zhu, Y. Guo, Y. Zhang, Y. Ju, R. Feng, Y. Liu, Z. Chen, J. Zhou, *Sol. Energy Mater. Sol. Cells* **2019**, *193*, 237.
[48] X. Chen, H. Gao, M. Yang, W. Dong, X. Huang, A. Li, C. Dong, G. Wang, *Nano Energy* **2018**, *49*, 86.
[49] D. Liu, C. Lei, K. Wu, Q. Fu, *ACS Nano* **2020**, *14*, 15738.
[50] J. Yang, L.-S. Tang, R.-Y. Bao, L. Bai, Z.-Y. Liu, W. Yang, B.-H. Xie, M.-B. Yang, *J. Mater. Chem. A* **2016**, *4*, 18841.
[51] J. Qiu, X. Fan, Y. Shi, S. Zhang, X. Jin, W. Wang, B. Tang, *J. Mater. Chem. A* **2019**, *7*, 21371.
[52] W. Wang, B. Tang, B. Ju, Z. Gao, J. Xiu, S. Zhang, *J. Mater. Chem. A* **2017**, *5*, 958.
[53] J. Yang, L.-S. Tang, L. Bai, R.-Y. Bao, Z. Liu, B.-H. Xie, M.-B. Yang, W. Yang, *ACS Sustainable Chem. Eng.* **2018**, *6*, 6761.
[54] X. Chen, Z. Tang, H. Gao, S. Chen, G. Wang, *Iscience* **2020**, *23*, 101208.
[55] H. Gao, J. Wang, X. Chen, G. Wang, X. Huang, A. Li, W. Dong, *Nano Energy* **2018**, *53*, 769.
[56] Y. Zhang, M. M. Umair, S. Zhang, B. Tang, *J. Mater. Chem. A* **2019**, *7*, 22218.
[57] C. Wang, G. Zhang, S. Ge, T. Xu, Y. Ji, X. Yang, Y. Leng, *Nature* **2016**, *529*, 515.
[58] X. Yang, T. Liu, Y. Gao, S. Ge, Y. Leng, D. Wang, C. Wang, *Joule* **2019**, *3*, 3002.
[59] X. Hu, Y. Zheng, D. A. Howey, H. Perez, A. Foley, M. Pecht, *Prog. Energy Combust. Sci.* **2020**, *77*, 100806.